micromachines

MDPI

Article

Design and Algorithm Verification of a Gyroscope-Based Inertial Navigation System for Small-Diameter Spaces in Multilateral Horizontal Drilling Applications

Tao Li [1,2,*], Gannan Yuan [1], Haiyu Lan [1,3] and Martin Mintchev [2]

Received: 29 August 2015; Accepted: 20 November 2015; Published: 9 December 2015
Academic Editor: Stefano Mariani

1 Marine Navigation Research Institute, College of Automation, Harbin Engineering University, No. 145 Nan Tong Street, Harbin 150001, China; yuangannan@hrbeu.edu.cn
2 Low Frequency Instrumentation Laboratory, Department of Electrical and Computer Engineering, University of Calgary, Calgary, AB T2N 1N4, Canada; mintchev@ucalgary.ca
3 Department of Geomatics Engineering, University of Calgary, Calgary, AB T2N 1N4, Canada; hlan@ucalgary.ca
* Correspondence: taoli321@yahoo.com; Tel./Fax: +86-451-8251-9040

Abstract: In the recent years horizontal drilling (HD) has become increasingly important in oil and gas exploration because it can increase the production per well and can effectively rework old and marginal vertical wells. The key element of successful HD is accurate navigation of the drill bit with advanced measurement-while-drilling (MWD) tools. The size of the MWD tools is not significantly restricted in vertical wells because there is enough space for their installation in traditional well drilling, but the diameter of devices for HD must be restricted to less than 30 mm for some applications, such as lateral drilling from existing horizontal wells. Therefore, it is essential to design miniature devices for lateral HD applications. Additionally, magnetometers in traditional MWD devices are easily susceptible to complex downhole interferences, and gyroscopes have been previously suggested as the best avenue to replace magnetometers for azimuth measurements. The aim of this paper is to propose a miniature gyroscope-based MWD system which is referred to as miniature gyroscope-based while drilling (MGWD) system. A prototype of such MGWD system is proposed. The device consists of a two-axis gyroscope and a three-axis accelerometer. Miniaturization design approaches for MGWD are proposed. In addition, MGWD data collection software is designed to provide real-time data display and navigation algorithm verification. A fourth-order autoregressive (AR) model is introduced for stochastic noise modeling of the gyroscope and the accelerometer data. Zero velocity and position are injected into a Kalman filter as a system reference to update system states, which can effectively improve the state observability of the MGWD system and decrease estimation errors. Nevertheless, the azimuth of the proposed MGWD system is not observable in the Kalman filter, and reliable azimuth estimation remains a problem.

Keywords: MGWD; multilateral well; horizontal drilling; MWD; Kalman filter; AR model; quasi-stationary alignment; inertial sensor

1. Introduction

Horizontal directional wells offer large contact areas with oil- or gas-layered reservoirs, so horizontal directional drilling (HDD) can enhance the production and exploration rate of oil or gas. HDD technology enables successful oil or gas exploration under challenging environments, such as offshore zones, mountain areas, and even downtown places [1]. Currently, re-entry well drilling, one of the HDD technologies, can revitalize old and marginal wells by intercepting its multiple vertical fractures to optimize the oil or gas yield [2,3]. Multilateral well drilling is becoming increasingly more valuable in horizontal well exploration, both from the standpoint of reworking existing wellbores and with respect to drilling operations [4]. Multilateral drilling to the sides of an existing horizontal well can be regarded as a branching from the stem of the main horizontal drilling tree and, naturally, is characterized with much smaller diameters than traditional HD [5,6]. Therefore, significantly smaller-diameter navigation equipment is needed in such applications, reaching as low as 15 mm in diameter (Figure 1).

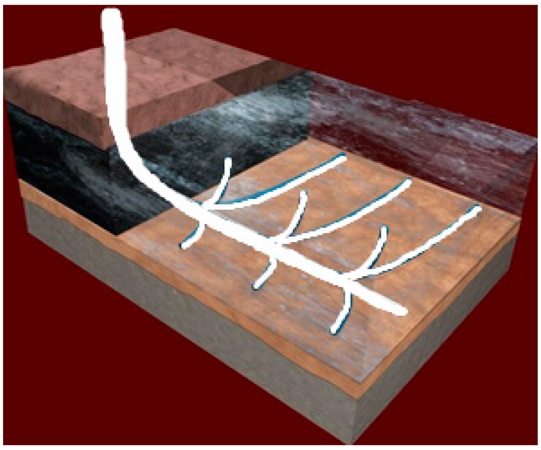

Figure 1. Multilateral horizontal drilling is characterized by small-diameter branches stemming from the main horizontal well tree trunk, thus significantly increasing the peripheral oil well output.

In multilateral horizontal drilling applications the navigation requirements become even more stringent compared to traditional MWD-based horizontal directional drilling. Traditional MWD HDD surveying tools determine the roll and the pitch of the drill bit by employing three-axe accelerometers and the azimuth of drill bit using three-axe magnetometers [7]. However, the precision of the magnetic surveying sensors is corrupted by several factors: (1) magnetometers are susceptible to external interferences caused by currents flowing in the atmosphere and solar winds, which can introduce independent errors distorting the calculation of the MWD toolset orientation [8]; (2) the presence of drilling fluids and debris downhole interacts with the earth magnetic field and further increases the azimuth error by up to 5° [9]; and (3) ferromagnetic interferences from the drill string induce large azimuth error which increases with the increase in the inclination angle and is especially significant when the well is drilled in the east/west direction [10,11]. In addition, randomly-located ore deposits in the vicinity of bottom-hole assembly (BHA) deteriorate survey quality due to strong, but intermittent magnetic interferences. One feasible approach to avoid these magnetic interferences is to enlarge the covering area of the non-magnetic drill collars of the BHA [12]. However, non-magnetic drill collars are characterized by their high cost, heavy weight, and relatively weak fracture, which is usually prone to failure. Gyroscope-based Inertial Navigation Systems (INS) can continuously provide position, velocity, and attitude of objects, such as submarines, airplanes, rockets, automobiles, *etc.*, relative to an initial point by a combination of gyroscopes and accelerometers [13]. Such systems can serve as an alternative to magnetometer-based surveying in downhole MWD. Since such INS is a type of dead-reckoning system which needs to integrate the outputs of inertial sensors for the calculation of orientation and position, INS is characterized by short-term high accuracy and long-term error accumulation [14]. Even high-accuracy INS operating in an unaided mode may produce 5000 ft. position error per hour due to sensor's error and bias accumulation [15]. Moreover, stochastic noise at the output of the gyroscopes additionally and significantly deteriorates the accuracy of this orientation solution, so building an appropriate gyroscope stochastic error model is pivotal in the quest to improve the overall quality of this navigation solution. In addition, it has to be noted that MWD systems, in particular, operate in very harsh downhole environments, making the utilization of gyroscopes downhole even more difficult, because their stochastic noise characteristics are not stable at different and dynamically changing temperatures and vibrations. However, advances in contemporary micro-electro-mechanical system (MEMS) technology enables the manufacturing of new generations of gyroscopes of smaller size, with excellent vibration immunity combined with high-temperature tolerance.

Gyroscopic multiple shot was firstly described in [16] which provided a series of photographic images showing the inclination and the direction of a well, but the measurements were not in real-time. Fiber optic gyroscope-based MWD surveying tool was proposed in [17], which was used to monitor the BHA's azimuth. A drilling BHA with a small-diameter rate gyroscope was deployed in [18] to reduce borehole position uncertainty under the influence of disturbing magnetic environments and near metal casings. The susceptibility of MEMS gyroscopes to shocks and vibrations was successfully tested in harsh downhole environments and a wavelet-denoising method was used to enhance the azimuth accuracy of the BHA [19]. A MEMS gyroscope guidance system was designed for ultra-deep-water applications to shorten the drilling response time and to decrease magnetic impact [20]. Nevertheless, BHA navigation errors caused by the bias in MEMS gyroscopes are greatly increased in harsh environments if compensatory external adjusting is lacking. Zero velocity update (ZUPT) alignment has been introduced to compensate for MEMS errors [21] and this method limited the position error to 40 m during 90 min navigation with a Litton LTN90-100 inertial measurement unit. However, ZUPT alignment is time consuming and is useless for azimuth estimation [22]. Velocity matching alignment merges velocity measurements from GPS to Kalman filtering to estimate the orientation of objects [23]. The prerequisite to use this method is the availability of a GPS signal, but the radio signals cannot reach downhole. Therefore, In-drilling Alignment (IDA) was proposed to constrain the azimuth error which was estimated to be 25 times smaller than the error restriction in traditional magnetometer-based surveying [24,25]. Rotary-In-Drilling Alignment (R-IDA), a reduced version of the IDA, was recently proposed to minimize INS dynamic position and azimuth errors. In R-IDA, the BHA was installed on a rotating platform controlled by a stepper motor in the north-east plane associated with the azimuth angle [26]. However, IDA and R-IDA associated devices cannot be directly utilized in lateral HDD applications because of size limitations.

This paper presents the design and algorithm verification of a MGWD device for lateral HDD applications. The design requirements were defined as follows:

- The attitude error of the device should be less than 0.1° and the position error should be less than 1 m for 1000 m-deep wells.
- The device installs in a steel tube of 24-mm maximal diameter and the size of the three-dimensional device should be less than 150 mm × 150 mm × 10 mm (length, width and height).
- The temperature range of the device should be between 40 and 100 °C.
- The device should be able to perform well in a shock and vibration environment ranging up to 15 g RMS (5–500 Hz).

In order to meet the above design requirements, small-diameter and high temperature sensors were selected. Custom software was designed for MGWD data collection and algorithm implementation. The Allan variance method was utilized to test the error characteristics of all sensors in the designed MGWD system. The results from the autocorrelation function calculation for the gyroscopes and the accelerometers showed that the stochastic noise of the sensors cannot be simply modeled with the Gauss-Markov model, so a fourth-order autoregressive (AR) model was employed for the stochastic noise modeling of the sensors. The alignment method of the MGWD device utilized zero velocity together with zero position update and accurate Kalman filter state space equation was built in terms of the system dynamics for fine alignment. In addition, this paper discusses system stability and state observability of the developed laboratory model.

2. Fundamental Theory of Miniature Gyroscope-Based While Drilling (MGWD) System

2.1. Definition of Coordinate Frames

Body frame is an orthogonal axis aligned with roll, pitch, and azimuth of the objects [27]. The MGWD system in this paper uses right, forward, and up direction as the body frame indicated in Figure 2.

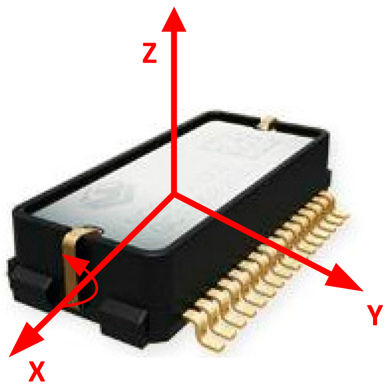

Figure 2. Definition of SCC1300-D04 body frame.

SCC1300-D04 (Murata Electronic Inc., College Station, PA, USA) is a combined gyroscope (*X*-axis) and three-axis accelerometer component [28], which main characteristics are shown in Table 1.

Table 1. SCC1300-D04 Performance.

Parameters	Gyroscope	Parameters	Accelerometer
Offset Short Term Instability	<2.1°/h	Offset Error	±70 mg
Angular Random Walk	$0.86°/\sqrt{h}$	Linearity Error	±40 mg
Noise Density	$0.02(°/\mathrm{s}/\sqrt{h})$	Noise	5–7 mg
Temperature	−40–+125 °C	Temperature	−40–+125 °C

2.2. MGWD System Navigation Solution

A two-axe gyroscope and three-axe accelerometer combine together in a MGWD system to provide the angular rate and acceleration for drill bit, respectively, while the attitude can be obtained by the integration of the angular rate. The two-axe gyroscope provides the angular rate of the MGWD system in the direction of right and down, respectively, while the angular rate for the forward direction can be assessed by the three-axes accelerometer because the velocity of downhole drill bit movements is slow (1 m/min). Figure 3 illustrates the details of the MGWD system attitude solution update. The roll (φ) of the MGWD system can be obtained based on the following equation [29]:

$$\varphi = -\arctan\left(\frac{\mathrm{f}_{\mathrm{ib},y}^{\mathrm{b}}}{\mathrm{f}_{\mathrm{ib},z}^{\mathrm{b}}}\right) \tag{1}$$

where $\mathrm{f}_{\mathrm{ib},y}^{\mathrm{b}}$, $\mathrm{f}_{\mathrm{ib},z}^{\mathrm{b}}$ are the *Y*-axis and Z-axis accelerometer outputs.

Hence, the angular rate incremental can be written during the period of t_k to t_{k+1} as:

$$\Delta\varphi = \varphi\,(t_{k+1}) - \varphi(t_k) \tag{2}$$

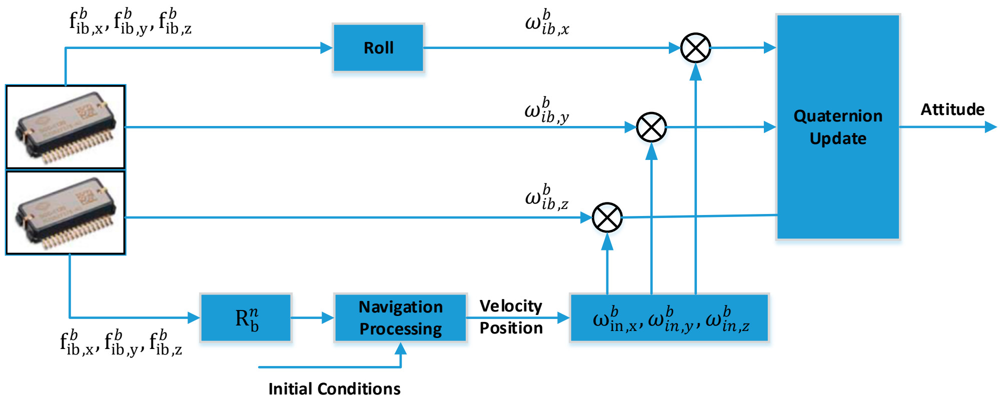

Figure 3. Miniature Gyroscope-Based While Drilling (MGWD) system attitude solution diagram.

Generally, the direction cosine matrix and quaternion can represent attitude information. In this paper, the rotation vector method is selected to update the quaternion attitude representation, as it occurs in the presence of a coning motion. The same approach is used to update the quaternion with a direction cosine matrix:

$$q^{n(k)}_{b(k)} = q^{n(k)}_{n(k-1)} q^{n(k-1)}_{b(k-1)} q^{b(k-1)}_{b(k)} \tag{3}$$

where $q^{n(k)}_{n(k-1)}$ is the quaternion in navigation frame update. $q^{b(k-1)}_{b(k)}$ is the quaternion in body frame update:

$$q^{n(k)}_{n(k-1)} = \begin{bmatrix} \cos \| 0.5\zeta_k \| \\ \frac{\sin \| 0.5\zeta_k \|}{\| 0.5\zeta_k \|} 0.5\zeta_k \end{bmatrix} \tag{4}$$

where, ζ_k has been updated previously by the following equation. $\|\|$ is the Euclidean norm.

$$\zeta_{k-1,k} = \int_{t_{k-1}}^{t_k} \omega^n_{in}(\tau)\, d\tau = \omega^n_{in,mid} \Delta t \tag{5}$$

$\omega^n_{in,mid}$ is the rotation rate of the navigation frame relative to the inertial frame at the midway of the internal $[t_{k-1}, t_k]$. Δt is the sampling time.

$$q^{b(k-1)}_{b(k)} = \begin{bmatrix} \cos \| 0.5\Lambda_k \| \\ \frac{\sin \| 0.5\zeta_k \|}{\| 0.5\Lambda_k \|} 0.5\Lambda_k \end{bmatrix} \tag{6}$$

Λ_k is the rotation vector, which can be updated by the following expression:

$$\Lambda_k = \Delta\theta_k + \frac{1}{12} \Delta\theta_{k-1} \times \Delta\theta_k \tag{7}$$

$\Delta\theta_k$ is the angular increment. $\times$ is the cross product.

$$\Delta\theta_k = f^b_{ib}\Delta t - \omega^b_{in} \tag{8}$$

where, f^b_{ib} are the accelerometer outputs and ω^b_{in} is the navigation frame angular rate with respect to the inertial frame referred to the body frame.

Hence, the direction cosine matrix (R^n_b) between the body frame and the navigation frame can be updated according to the following solution:

$$R^n_b = I + \frac{\sin \| \Lambda \|}{\| \Lambda \|} (\Lambda \times) + \frac{1 - \cos \| \Lambda \|}{\| \Lambda \|^2} (\Lambda \times)(\Lambda \times) \tag{9}$$

where I is the identity matrix and $(\Lambda\times)$ is the skew symmetric matrix of Λ.

$$(\Lambda\times) = \begin{bmatrix} 0 & -\Lambda_z & \Lambda_y \\ \Lambda_z & 0 & -\Lambda_x \\ -\Lambda_y & \Lambda_x & 0 \end{bmatrix} \tag{10}$$

2.3. MGWD System Error Model

The Kalman filter estimates the attitude, velocity and position error of the proposed MGWD system based on the system state equation. Equation (11) briefly illustrates the continuous time MGWD system state propagation.

$$\delta\dot{x} = \mathrm{F}\delta x + \mathrm{Gw} \tag{11}$$

where $\delta x = [\delta\phi\ \delta\theta\ \delta\psi\ \delta V_N\ \delta V_E\ \delta V_D\ \delta L\ \delta\lambda\ \delta h]^T$, in which $\delta\varphi$, $\delta\theta$ and $\delta\psi$ are roll, pitch, and azimuth errors, respectively. δV_N, δV_E and δV_D are north, east, and down velocity errors, respectively. δL, $\delta\lambda$ and δh are latitude, longitude, and height errors, respectively. G is the system noise matrix. F is the state transfer matrix which can be written as [30].

$$\mathrm{F} = \begin{bmatrix} F_{11} & F_{12} & F_{13} \\ F_{21} & F_{22} & F_{23} \\ F_{31} & F_{32} & F_{33} \end{bmatrix} \tag{12}$$

where

$$F_{11} = \begin{bmatrix} 0 & -\left(\omega_{ie}\sin\varphi + \frac{V_E}{R}\tan\varphi\right) & \frac{V_N}{R} \\ \omega_{ie}\sin\varphi + \frac{V_E}{R}\tan\varphi & 0 & \omega_{ie}\cos\varphi + \frac{V_E}{R} \\ -\frac{V_N}{R} & -\left(\omega_{ie}\cos\varphi + \frac{V_E}{R}\right) & 0 \end{bmatrix}$$

$$F_{12} = \begin{bmatrix} 0 & \frac{1}{R} & 0 \\ -\frac{1}{R} & 0 & 0 \\ 0 & -\frac{\tan\varphi}{R} & 0 \end{bmatrix}$$

$$F_{13} = \begin{bmatrix} \omega_{ie}\sin\varphi & 0 & -\frac{V_E}{R^2} \\ 0 & 0 & \frac{V_N}{R^2} \\ -\omega_{ie}\cos\varphi - \frac{V_E}{R\cos^2\varphi} & 0 & \frac{V_E\tan\varphi}{R^2} \end{bmatrix}$$

$$F_{21} = \begin{bmatrix} 0 & -f_D & f_E \\ f_D & 0 & -f_N \\ -f_E & f_N & 0 \end{bmatrix}$$

$$F_{22} = \begin{bmatrix} \frac{V_D}{R} & -2\left(\omega_{ie}\sin\varphi + \frac{V_E}{R}\tan\varphi\right) & \frac{V_N}{R} \\ 2\omega_{ie}\sin\varphi + \frac{V_E}{R}\tan\varphi & \frac{1}{R}(V_N\tan\varphi + V_D) & \omega_{ie}\cos\varphi + \frac{V_E}{R} \\ -\frac{2V_N}{R} & -2\left(\omega_{ie}\cos\varphi + \frac{V_E}{R}\right) & 0 \end{bmatrix}$$

$$F_{23} = \begin{bmatrix} -V_E\left(\omega_{ie}\cos\varphi + \dfrac{V_E}{R\cos^2\varphi}\right) & 0 & \dfrac{1}{R^2}\left(V_E^2\tan\varphi - V_NV_D\right) \\ 2\omega_{ie}\left(V_N\cos\varphi - V_D\sin\varphi\right) + \dfrac{V_NV_E}{R\cos^2\varphi} & 0 & -\dfrac{V_E}{R^2}\left(V_N\tan\varphi + V_D\right) \\ 2\omega_{ie}V_E\sin\varphi & 0 & \dfrac{1}{R^2}\left(V_N^2 + V_E^2\right) \end{bmatrix}$$

$$F_{31} = \begin{bmatrix} 0 & 0 & 0 \\ 0 & 0 & 0 \\ 0 & 0 & 0 \end{bmatrix}$$

$$F_{32} = \begin{bmatrix} \dfrac{1}{R} & 0 & 0 \\ 0 & \dfrac{1}{R\cos\varphi} & 0 \\ 0 & 0 & -1 \end{bmatrix}$$

$$F_{33} = \begin{bmatrix} 0 & 0 & -\dfrac{V_N}{R^2} \\ \dfrac{V_E\tan\varphi}{R\cos\varphi} & 0 & -\dfrac{V_E}{R^2\cos\varphi} \\ 0 & 0 & 0 \end{bmatrix}$$

The above equations imply that the attitude, velocity, and position errors are coupled together [31].

2.4. Kalman Filter Theory

Kalman filtering is a minimum variance estimate in the recursive form and in the present case it is a linear, discrete time, system of finite dimensions [32]. It assumes that all variables are Gaussian and system noise and measurement noise are uncorrelated. The goal of the Kalman filter is to estimate the system state based on the knowledge of the system dynamics and the availability of separate noise measurements [33]. The discrete Kalman filter can be given as follows:

$$x_k = \Phi_{k-1}x_{k-1} + \Gamma_{k-1}w_{k-1} \tag{13}$$

$$z_k = H_k x_k + v_k \tag{14}$$

where x_k is system state, which is same as the MGWD system state δx described in Equation (11). Γ_{k-1} is system noise matrix, which is the discretization form of G. Φ_{k-1} is system state transfer matrix, which is discrete form of F [34].

$$\Phi_{k-1} = e^{F\Delta t} \approx I + F\Delta t \tag{15}$$

$$\Gamma_{k-1} = \int_0^{\Delta t} e^{(t_k-\tau)F}Gd\tau = e^{F\Delta t}\int_0^{\Delta t} e^{-F\tau}d\tau G \approx e^{F\Delta t}\left(I - e^{-F\Delta t}\right)F^{-1}G = G\Delta t \tag{16}$$

z_k represents the system measurements at time k, and H_k is the measurement matrix. w_{k-1} and v_k are the system noise and measurement noise, respectively, in which: $E[w_kw_j^T] = Q_k\delta_{kj}$, $E[v_kv_j^T] = R_k\delta_{kj}$, $E[w_kv_j^T] = 0$. w_k and v_k are zero mean, uncorrelated white noise and their covariance matrices are Q_k and R_k, respectively. δ_{kj} is the Kronecker's delta. The Kalman filter mainly consists of two update periods: time update and measurement update.

Time update equation can be given as follows:

$$x_k^- = \Phi_{k-1}x_{k-1} \tag{17}$$

$$P_k^- = \Phi_{k-1}P_{k-1}\Phi_{k-1}^T + \Gamma_{k-1}Q_{k-1}\Gamma_{k-1}^T \tag{18}$$

Measurement update equation can then be expressed as:

$$K_k = P_k^- H_k^T \left(H_k P_k^- H_k^T + R_k \right)^{-1} \tag{19}$$

where K_k is the Kalman filter gain.

$$x_k = x_k^- + K_k \left(z_k - H_k x_k^- \right) \tag{20}$$

$$P_k = (I - K_k H_k) P_k^- (I - K_k H_k)^T + K_k R_k K_k^T \tag{21}$$

The initial condition (x_0,P_0) of the Kalman filter will not have an impact upon the filter convergence, and Q_k, R_k just affect the final convergence value of Kalman filter. Moreover, the Kalman filter will converge to some value if the system is completely controllable and observable; in other words, if the controllable and the observable matrix (M = ctrb(F,G)) and N = obsv(F,H)) are full rank [35,36].

3. MGWD System Design and Testing

3.1. MGWD System Design

Minimal diameter is an essential feature of the proposed MGWD system. To minimize the dimensions of the MGWD system, a two-axis gyroscope and three-axis accelerometer are combined together to provide attitude, velocity, and position information for the drill bit and one gyroscope is placed into the cut part of the microcontroller circuit board. The layout and the dimensions of the MGWD system are illustrated in Figure 4. The system hardware is composed of the azimuth gyroscope circuit board, pitch gyroscope circuit board, and microcontroller circuit board. The boards are connected by a micro header (pitch: 1.27 mm). In addition, SMD (Surface-Mount Device) 0402 footprint (1 mm × 5 mm) resistors and capacitors are selected as peripheral electronic components and they are placed on both sides of the circuit boards to reduce the device dimensions. The entire dimensions of the MGWD system are (121.913 mm × 17.907 mm × 10 mm) (length, width and height).

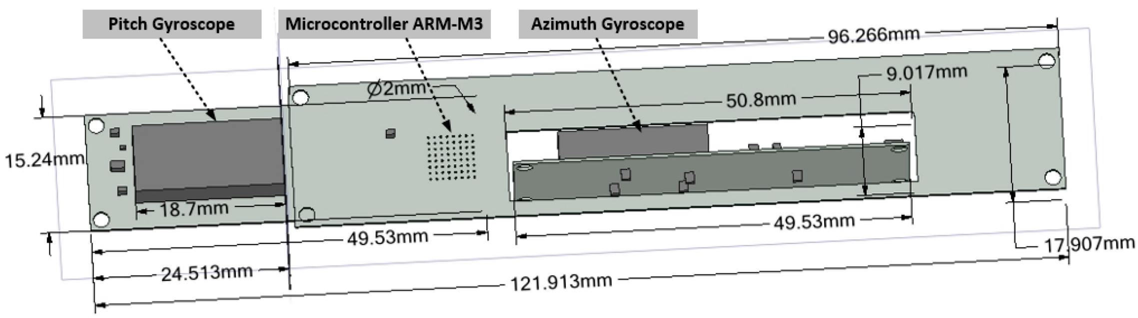

Figure 4. MGWD system layout and dimensions.

The system sample rate of the MGWD device is controlled to 20 Hz because of the low equipment angular change rate. The data exchange protocol between the microcontroller and the two gyroscopes is serial peripheral interface (SPI) which includes a single master (the microcontroller) and two slaves (the two gyroscopes).

The data communication codes are programmed in the environment of IAR Embedded Workbench with the C programming language and the codes are downloaded to the flash memory of the microcontroller through a USB interface with a XDS100/200/ICDI emulator. The data output baud rate is set to 115,200 bits/s.

MGWD data collection software interface (Figure 5) is designed with the XAML programming language in WPF environment and data collection and processing codes are programmed with the

C# language which consists of six stack panels: menu, serial port, initialization, data count, timer, and data display.

The menu includes file control, parameter setting, and system control and help information. The data display part is composed of a horizontal sensor (azimuth) and vertical (pitch) sensor original data display, horizontal sensor original data curve line display, vertical sensor original data curve line display, and calibration result display. The user interface design flow diagram of the software is shown in Figure 6. The software process flow diagram can be found in Figure 7, which presents the software development processes and the application methods utilized.

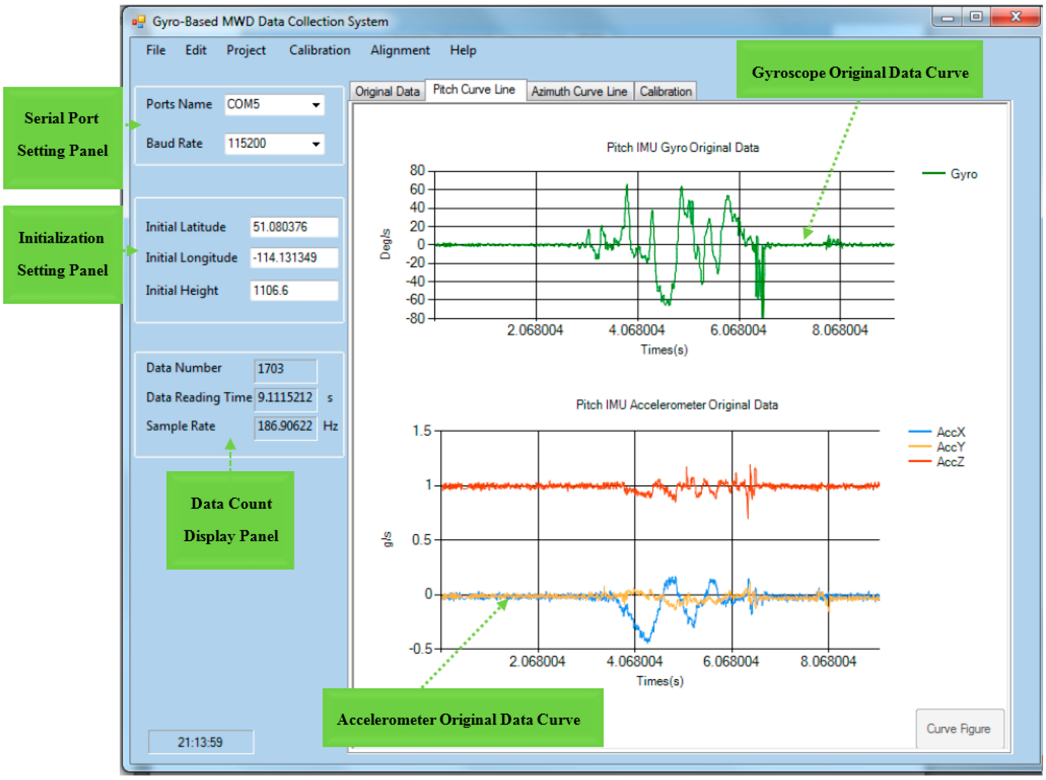

Figure 5. MGWD data collection software interface.

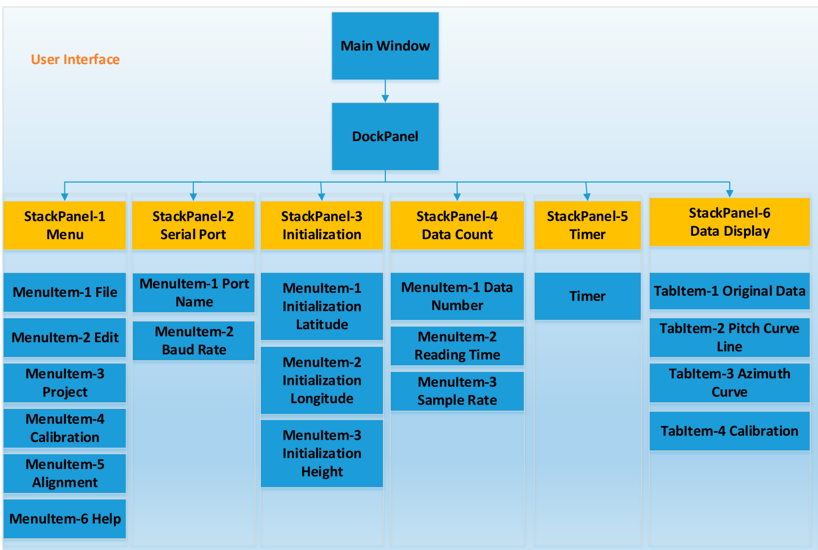

Figure 6. User interface design flow diagram.

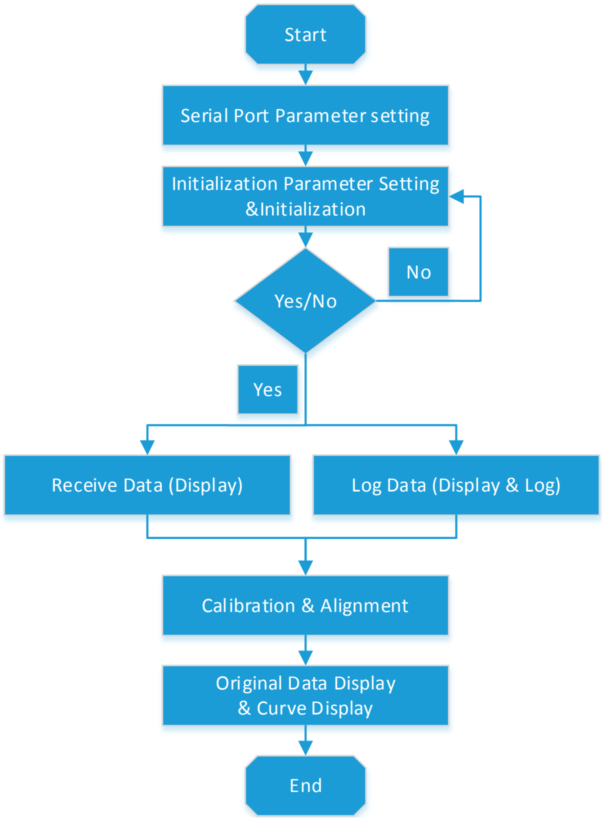

Figure 7. MGWD data collection software process flow diagram.

3.2. MGWD System Test

3.2.1. Allan Variance Analysis

The Allan variance approach is selected to test the sensor stochastic noise characteristic. It is a method of analyzing the time sequence to extracts the intrinsic noise in the system as a function of the average time. A *Y*-axis gyroscope and a *Z*-axis accelerometer are used as an example to explain the meaning of Allan variance. 8 h and 20 min static data with 20 Hz sample rate are collected for inertial sensor Allan variance analysis.

Angular Random Walk (ARW) is a high frequency white noise exhibited in noise sequences associated with MEMS devices by integrating 1-s time periods. In other words, the ARW value can be obtained by reading the slope line for a time of 1 s. Conversely, the contribution of the white noise to the inertial sensor error ($e_{\text{white\_noise}}$) can be quantified by the following Equation (22):

$$e_{\text{white\_noise}} = \text{ARW} \times \sqrt{t} \tag{22}$$

where t is the integration time for the inertial sensor white noise. Bias stability of the inertial sensor illustrates how the bias changes over a certain period of time due to the flicker noise in the electronics [37]. The bias stability calculates the minimum average change in consecutive inertial sensor measurements while analyzing the consecutive time-varying samples. The valley bottom with the zero slope represents bias stability. *Y*-axis gyroscope and *Z*-axis accelerometer noise Allan variances are shown in Figure 8 and ARW and bias stability of the inertial sensors are summarized in Table 2. Bias stability of the inertial sensor illustrates how the bias changes over a certain period of time due to the flicker noise in the electronics [37]. The bias stability calculates the minimum average change in consecutive inertial sensor measurements while analyzing the consecutive time-varying samples. The valley bottom with the zero slope represents bias stability. *Y*-axis gyroscope and *Z*-axis accelerometer noise Allan variances are shown in Figure 8, and ARW and bias stability of the inertial sensors are summarized in Table 2.

Table 2. Results of Allan variance analysis.

Sensor	Angular Random Walk	Bias Stability
Y-Axis Gyroscope	0.004466835 ($^\circ$/h/$\sqrt{\text{Hz}}$)	0.00120876 ($^\circ$/s)
Sensor	**Velocity Random Walk**	**Bias Stability**
Z-Axis Accelerometer	0.052257815 (m/s/$\sqrt{\text{h}}$)	0.000554625 m/s^2

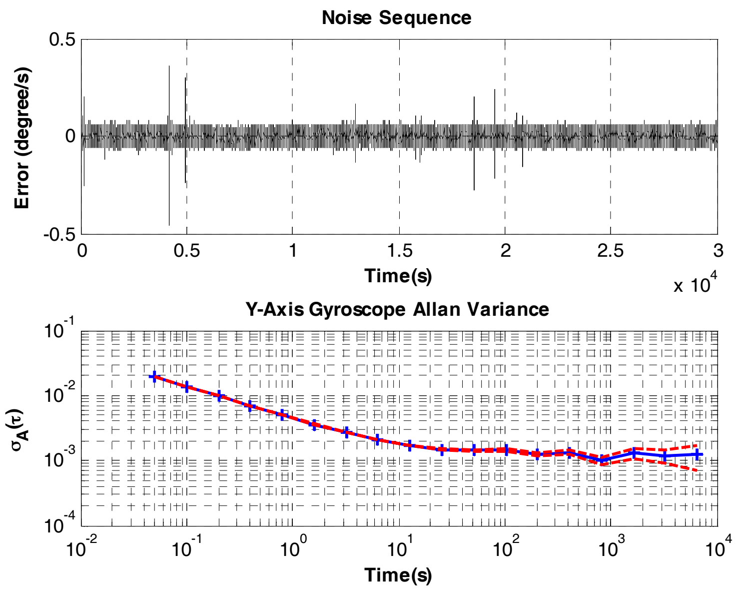

(**a**)

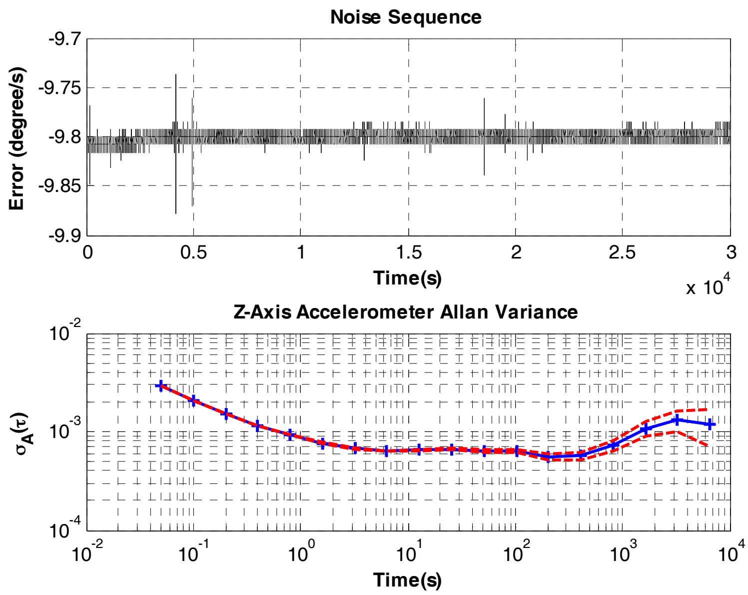

(**b**)

Figure 8. (**a**) *Y*-Axis Gyroscope Allan variance analysis; and (**b**) *Z*-Axis accelerometer Allan variance analysis.

3.2.2. Stochastic Error Model

The INS error includes deterministic error and stochastic error. The deterministic error can be eliminated from the raw measurements by a properly selected calibration method. In this paper, the six-position calibration method is employed to calculate the system deterministic error [38]. The calibration results are shown in Table 3.

Table 3. Six position calibration results.

Axis	Gyroscope Calibration Error (°/s)	Accelerometer Calibration Error (m/s^2)
X-Axis	−0.021121495327103	−0.007083371298406
Y-Axis	−0.002242990654206	−0.020187699316629
Z-Axis	−0.016448598130841	0.002405466970394

However, it is difficult to remove the stochastic error easily by any physical method, while a precise mathematical model can solve the problem far more effectively. Although a first-order Gauss-Markov model can accurately build a stochastic model for navigation-grade INS systems, low-cost INS systems need a more precise stochastic model to ensure precision of the navigation solution because of the complex noise components existing in it [39]. The autocorrelation results (Figure 9) from the sensor stochastic error calculations show that the errors cannot be simply modeled by a first-order Gauss-Markov model.

Hence, building an accurate stochastic error model for the MGWD system under the conditions of no external reference aid information is a significant necessity for downhole drilling applications. An AR model is selected for system noise modeling, which assumes that present observations z_k are related to the past observations and Gaussian white noise ϵ_{w} [40,41].

$$z_k = -\sum_{\mathrm{i}=1}^{\mathrm{p}} \mathrm{a_i} z_{k-\mathrm{i}} + \epsilon_{\mathrm{w}} \tag{23}$$

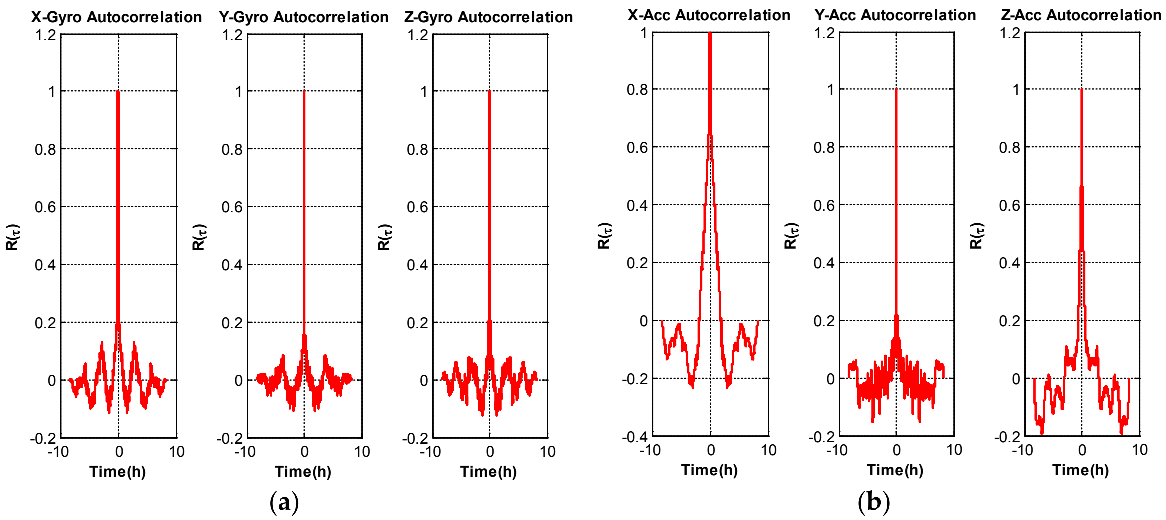

Figure 9. (**a**) Gyroscope autocorrelation results; and (**b**) accelerometer autocorrelation results.

Typically, three methods can be used to estimate AR model coefficients $\mathrm{a_i}$: the Yule-Walker method, covariance method, and maximum entropy spectral estimation. The Yule-Walker method uses estimation of autocorrelation of the measurements to solve the model coefficients as well as the variance of white noise. The autocorrelation function of the AR model is illustrated by Equation (24).

The key point to estimate the AR model coefficients utilizing the Yule-Walker approach is to solve the following linear equation:

$$R_{zz}(k) = \sum_{i=1}^{p} a_i R_{zz}(k - i) \tag{24}$$

The autocorrelation function R_{zz} of the AR process is obtained from Equation (24) by a simple calculation. The white noise variance is given by Equation (25):

$$\sigma_w^2 = \sum_{i=1}^{p} a_i R_{zz}(-i) \tag{25}$$

It has been shown that the Yule-Walker method is applicable to estimate short data records but it usually brings errors during estimation of AR model coefficients [38]. Similarly to the Yule-Walker approach, the covariance method solves the AR coefficients by the following equation:

$$-C_{zz}(0, i) = \sum_{i=1}^{p} a_i C_{zz}(i, k) \tag{26}$$

where $C_{zz}(0,i)$ is the sample covariance sequence and $C_{zz}(i,k)$ are the coefficients of the sample covariance matrix. Burg method is also related to maximum entropy estimate, which minimizes the forward and backward prediction error energy in the least squares sense. The details about this method were illustrated in a previous paper [38]. In this paper, the fourth-order AR model coefficients are calculated by the Yule-Walker method. Tables 4 and 5 show the statistic noise AR model coefficients for all inertial sensors. The AR model coefficients of the *X*-axis gyroscope are obtained according to the angular rate calculated by the 3-axes accelerometer. In the following table, a_1, a_2, a_3, a_4 are the AR model coefficients and $\beta_{f,0}$ and $\beta_{w,0}$ are the AR model prediction mean square errors of the three-axes accelerometer and the three-axes gyroscope (with the *X*-axis gyroscope data calculated from the three-axes accelerometer input as previously explained).

Table 4. Fourth order AR model coefficients of the three-axe accelerometer.

Axis	a_1	a_2	a_3	a_4	$\beta_{f,0}$
X-Axis Accelerometer	0.3308	−0.0995	0.2036	0.3347	0.0034
Y-Axis Accelerometer	0.3307	−0.1118	0.1956	0.3350	2.0947×10^{-4}
Z-Axis Accelerometer	0.1249	−0.0801	0.0382	0.0724	3.3090×10^{-6}

Table 5. Fourth order AR model coefficients of a three-axe accelerometer.

Axis	b_1	b_2	b_3	b_4	$\beta_{w,0}$
X-Axis Gyroscope	−0.0866	−0.5159	−0.0947	−0.1270	2.2871×10^{-7}
Y-Axis Gyroscope	−0.8466	−0.1105	0.2948	−0.1642	7.1662×10^{-7}
Z-Axis Gyroscope	−0.2683	−0.0026	0.0192	−0.3496	6.9822×10^{-7}

3.2.3. MGWD System Alignment

The basic principle of a strapdown inertial navigation system is to deduce navigation parameters (position, velocity, and attitude) in accordance with their initial value. The initial attitude can be measured automatically within the framework of the initial alignment rather than with the assistance of an external information source. Instead of using such external assistance, a zero velocity update (ZUPT) can be performed by stopping the system [13]. However, the initial position of the system has to be obtained by external knowledge, such as GPS or a landmark point. The purpose of coarse alignment is to build the relationship between the measurement frame where original sensor outputs are collected and the computation frame where velocity, position, and attitude of the actual MWD system are calculated. In other word, coarse alignment is used as the initializing the transformation matrix of attitude angles between the measurement frame and the computation frame.

MWD body frame is chosen as the measurement frame and the geographic frame is chosen as the calculation frame in this paper. Two major coarse alignment methods in quasi stationary conditions have been presented in previous research, gyro-compassing and analytical alignment approach.

Figure 10 illustrates the relationship between the geographic frame and the body frame using the gyro-compassing method. Briefly, searching the angle between the geographic frame ($X_{\rm n}$, $Y_{\rm n}$, $Z_{\rm n}$) and the body frame ($X_{\rm b}$, $Y_{\rm b}$, $Z_{\rm b}$) is the purpose of the coarse alignment. In general, the geographic coordinate frame can be transformed into the body coordinate frame through three times rotation, namely:

$$\mathrm{X_n},\ Y_n,\ Z_n\ (\boldsymbol{Z-Axis}) - \rightarrow X_A,\ Y_A,\ Z_A\ (\boldsymbol{Y-Axis}) - \rightarrow X_p,\ Y_p, Z_p\ (\boldsymbol{Y-Axis}) - \rightarrow (X_b,\ Y_b, Z_b)$$

where, ($X_{\rm A}$, $Y_{\rm A}$, $Z_{\rm A}$) and ($X_{\rm P}$, $Y_{\rm P}$, $Z_{\rm P}$) are the intermediate coordinates transiting from the geographic frame to the body frame. From geometrical point of view, the tilts between $X_{\rm n}$, $Y_{\rm n}$ and $X_{\rm b}$, $Y_{\rm b}$ equal to the pitch and the roll of the MGWD system, respectively.

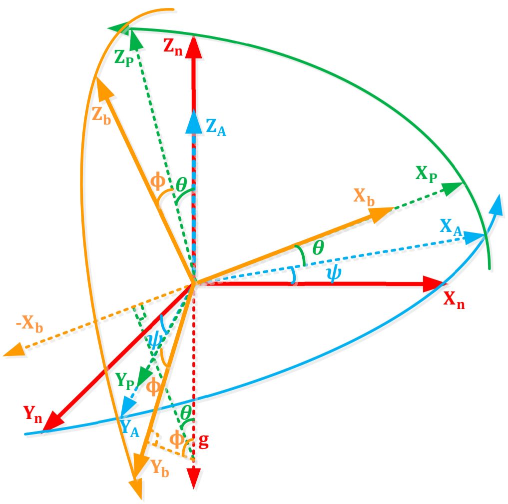

Figure 10. Geometrical and rotational relationships between the body frame and the geographic frame for gyro-compassing alignment.

The following formulas present the initial roll (ϕ), pitch (θ) and azimuth (ψ) based on their geometrical relationships illustrated on Figure 10 [42].

$$\sin\phi = \frac{f^{b}_{ib,y}}{g} \tag{27}$$

$$\sin\theta = -\frac{f^{b}_{ib,x}}{g} \tag{28}$$

$$\tan\psi = -\frac{\omega^{b}_{ib,x}}{\omega^{b}_{ib,y}} \tag{29}$$

This paper chooses an analytical alignment method collecting 5-s data to provide the initial attitude navigation parameters calculation. This analytical alignment method directly utilizes the knowledge of gravity (g), earth rotation rate (ω^{n}_{ie}), and their cross-product ($g \times \omega_{ie}$) to compute the transformation matrix R_b^n [43]. The analytical Coarse Alignment equation is listed in the following Equation (30).

$$R_b^n = \begin{bmatrix} (g^n)^T \\ (\omega_{ie}^n)^T \\ (g^n \times \omega_{ie}^n)^T \end{bmatrix}^{-1} \begin{bmatrix} (g^b)^T \\ (\omega_{ie}^b)^T \\ (g^b \times \omega_{ie}^b)^T \end{bmatrix} \\ = \begin{bmatrix} \frac{\omega_{ib,x}^b}{\omega_{ie}\cos\varphi} - \frac{f_{ib,x}^b \sin\varphi}{g\cos\varphi} & \frac{\omega_{ib,y}^b}{\omega_{ie}\cos\varphi} - \frac{f_{ib,y}^b \sin\varphi}{g\cos\varphi} & \frac{\omega_{ib,z}^b}{\omega_{ie}\cos\varphi} - \frac{f_{ib,z}^b \sin\varphi}{g\cos\varphi} \\ \frac{-f_{ib,y}^b \omega_{ib,z}^b + f_{ib,z}\omega_{ib,y}^b}{g\omega_{ie}\cos\varphi} & \frac{f_{ib,x}^b \omega_{ib,z}^b - f_{ib,z}\omega_{ib,x}^b}{g\omega_{ie}\cos\varphi} & \frac{-f_{ib,x}^b \omega_{ib,y}^b + f_{ib,y}\omega_{ib,x}^b}{g\omega_{ie}\cos\varphi} \\ -\frac{f_{ib,x}^b}{g} & -\frac{f_{ib,y}^b}{g} & -\frac{f_{ib,z}^b}{g} \end{bmatrix} \tag{30}$$

where $g^n = [0 \ \ 0 \ \ g]^T$, $\omega_{ie}^n = [\omega_{ie}\cos\varphi \ \ 0 \ \ -\omega_{ie}\sin\varphi]^T$, $g^b = -\left[f_{ib,x}^b \ \ f_{ib,y}^b \ \ f_{ib,z}^b\right]^T$, and $\omega_{ie}^b = \left[\omega_{ib,x}^b \ \ \omega_{ib,y}^b \ \ \omega_{ib,z}^b\right]^T$.

The coarse alignment results for roll, pitch, and azimuth are: −0.8061°, 0.5371° and −150.9636°, respectively. In this paper, the quasi-stationary fine alignment method is selected to compensate the MGWD system error. The system state variables (attitude, velocity, position, gyroscope bias, and accelerometer bias) are estimated by a Kalman filter with measurements of zero velocity and position. The Kalman filter is an estimator for linear systems, but modeling the system random noise by a fourth-order AR model violates the linearity precondition for Kalman filtering. To address this issue, the fourth-order AR model is decomposed into four first-order difference equations by defining four accelerometer random noise middle state variables Υ_1, Υ_2, Υ_3, Υ_4. According to Equation (23), the fourth-order AR models of gyroscope bias and accelerometer bias disturbed by white noise can be written in the following form [44]:

$$\delta f_k = -a_1\delta f_{k-1} - a_2\delta f_{k-2} - a_3\delta f_{k-3} - a_4\delta f_{k-4} + \beta_{f,0}w \tag{31}$$

$$\delta\omega_k = -b_1\delta\omega_{k-1} - b_2\delta\omega_{k-2} - b_3\delta\omega_{k-3} - b_4\delta\omega_{k-4} + \beta_{\omega,0}w \tag{32}$$

where the subscripts k, k−1, k−2, k−3 represent discrete sampled time moments k, k−1, k−2, k−3 respectively.

The middle state variables are defined as follows:

$$\Upsilon_{1,k} = \delta f_{k-3} \tag{33}$$

$$\Upsilon_{2,k} = \delta f_{k-2} \tag{34}$$

$$\Upsilon_{3,k} = \delta f_{k-1} \tag{35}$$

$$\Upsilon_{4,k} = \delta f_k \tag{36}$$

Therefore, the Equation (31) can be decomposed into 4 first-order difference equations as:

$$\Upsilon_{1,k} = \Upsilon_{2,k-1} \tag{37}$$

$$\Upsilon_{2,k} = \Upsilon_{3,k-1} \tag{38}$$

$$\Upsilon_{3,k} = \Upsilon_{4,k-1} \tag{39}$$

$$\Upsilon_{4,k} = -a_1\,\Upsilon_{1,\,k-1} - a_2\,\Upsilon_{2,\,k-1} - a_3\,\Upsilon_{3,\,k-1} - a_4\,\Upsilon_{4,\,k-1} + \beta_{f,0}w \tag{40}$$

Specifically, the above Equation can be written in the form of state space equation as:

$$\begin{bmatrix} \Upsilon_{1,k} \\ \Upsilon_{2,k} \\ \Upsilon_{3,k} \\ \Upsilon_{4,k} \end{bmatrix} = \begin{bmatrix} 0 & 1 & 0 & 0 \\ 0 & 0 & 1 & 0 \\ 0 & 0 & 0 & 1 \\ -\mathrm{a}_1 & -\mathrm{a}_2 & -\mathrm{a}_3 & -\mathrm{a}_4 \end{bmatrix} \begin{bmatrix} \Upsilon_{1,k-1} \\ \Upsilon_{2,k-1} \\ \Upsilon_{3,k-1} \\ \Upsilon_{4,k-1} \end{bmatrix} \tag{41}$$

Similarly, by defining the gyroscope random noise middle state variables Θ_1, Θ_2, Θ_3, Θ_4, the state space equation for the gyroscope random noise AR model can be written as:

$$\begin{bmatrix} \Theta_{1,k} \\ \Theta_{2,k} \\ \Theta_{3,k} \\ \Theta_{4,k} \end{bmatrix} = \begin{bmatrix} 0 & 1 & 0 & 0 \\ 0 & 0 & 1 & 0 \\ 0 & 0 & 0 & 1 \\ -\mathrm{b}_1 & -\mathrm{b}_2 & -\mathrm{b}_3 & -\mathrm{b}_4 \end{bmatrix} \begin{bmatrix} \Theta_{1,k-1} \\ \Theta_{2,k-1} \\ \Theta_{3,k-1} \\ \Theta_{4,k-1} \end{bmatrix} \tag{42}$$

The augmentation of the system state space model (Equation (11)) is written as follows:

$$\begin{bmatrix} \delta\dot{x}_{9\times1} \\ \dot{\Upsilon}_{12\times1} \\ \dot{\Theta}_{12\times1} \end{bmatrix} = \begin{bmatrix} \mathrm{F} & 0 & 0 \\ 0 & \mathrm{F}_{\mathrm{fw}} & 0 \\ 0 & 0 & \mathrm{F}_{\omega\mathrm{w}} \end{bmatrix}_{33\times33} \begin{bmatrix} \delta x \\ \Upsilon \\ \Theta \end{bmatrix} + \begin{bmatrix} \mathrm{G} & 0 & 0 \\ 0 & \beta_{\mathrm{f}} & 0 \\ 0 & 0 & \beta_{\omega} \end{bmatrix}_{33\times33} \mathrm{w} \tag{43}$$

where

$$\mathrm{F}_{\mathrm{fw}} = \begin{bmatrix} \mathrm{F}_{\mathrm{fw},x} & 0 & 0 \\ 0 & \mathrm{F}_{\mathrm{fw},y} & 0 \\ 0 & 0 & \mathrm{F}_{\mathrm{fw},z} \end{bmatrix}$$

$$\beta_{\mathrm{f}} = \begin{bmatrix} \beta_{\mathrm{f0},x} & 0 & 0 \\ 0 & \beta_{\mathrm{f0},y} & 0 \\ 0 & 0 & \beta_{\mathrm{x0},z} \end{bmatrix}$$

$$\mathrm{F}_{\omega\mathrm{w}} = \begin{bmatrix} \mathrm{F}_{\omega\mathrm{w},x} & 0 & 0 \\ 0 & \mathrm{F}_{\omega\mathrm{w},y} & 0 \\ 0 & 0 & \mathrm{F}_{\omega\mathrm{w},z} \end{bmatrix}$$

$$\beta_{\omega} = \begin{bmatrix} \beta_{\omega0,x} & 0 & 0 \\ 0 & \beta_{\omega0,y} & 0 \\ 0 & 0 & \beta_{\omega0,z} \end{bmatrix}$$

F_{fw} and $\mathrm{F}_{\omega\mathrm{w}}$ are the transfer matrices of the AR model and β_{f} and β_{ω} are the AR model predicts the mean square errors for the accelerometer and the gyroscope, respectively. The subscripts x, y and z represent the X-axis, Y-axis and Z-axis, respectively. The specific parameters of Equation (43) are illustrated in Appendix A. γ and Θ are the three-axes accelerometer random noise and the three-axes gyroscope random noise, respectively, and the random noises of each axis are modeled by a fourth-order AR model. γ and Θ are given as the following matrices:

$$\Upsilon = \left[\Upsilon_{1,x},\ \Upsilon_{2,x},\ \Upsilon_{3,x},\ \Upsilon_{4,x},\ \Upsilon_{1,y},\ \Upsilon_{2,y},\ \Upsilon_{3,y},\ \Upsilon_{4,y},\ \Upsilon_{1,z},\ \Upsilon_{2,z},\ \Upsilon_{3,z},\ \Upsilon_{4,z}\right]^{\mathrm{T}} \tag{44}$$

$$\Theta = \left[\Theta_{1,x},\ \Theta_{2,x},\ \Theta_{3,x},\ \Theta_{4,x},\ \Theta_{1,y},\ \Theta_{2,y},\ \Theta_{3,y},\ \Theta_{4,y},\ \Theta_{1,z},\ \Theta_{2,z},\ \Theta_{3,z},\ \Theta_{4,z}\right]^{\mathrm{T}} \tag{45}$$

where $\Upsilon_{\mathrm{i},x}$, $\Upsilon_{\mathrm{i},y}$, $\Upsilon_{\mathrm{i},z}$ and $\Theta_{\mathrm{i},x}$, $\Theta_{\mathrm{i},y}$, $\Theta_{\mathrm{i},z}$, i = 1,2,3,4 represent the defined state variables of the three-axes accelerometer and three-axes gyroscope respectively.

Therefore, the augmentation of the system state space model in Equation (43) can be rewritten in a discrete system form as:

$$X_k = \Phi_{k-1}X_{k-1} + \Gamma_{k-1}\mathrm{w}_{k-1}$$

where X_k and X_{k-1} are the augmentation system state variables at sampled time k and $k-1$, namely, $X_k = [\delta x, \Upsilon, \Theta]^{\mathrm{T}}$. The system state transfer matrix $\Phi_{k-1} = \begin{bmatrix} \mathrm{F} & 0 & 0 \\ 0 & \mathrm{F_{fw}} & 0 \\ 0 & 0 & \mathrm{F_{\omega w}} \end{bmatrix}$ and the system noise matrix $\Gamma_{k-1} = \begin{bmatrix} \mathrm{G} & 0 & 0 \\ 0 & \beta_\mathrm{f} & 0 \\ 0 & 0 & \beta_\omega \end{bmatrix}$. To estimate the system state, the linear Kalman filter can be employed because the augmentation system state space model is now linearized. Although modeling white noise by AR model violates the assumption that the Kalman filter provides the optimal estimation for linear system disturbed by white noise, Kalman filter can still be performed in this context because the matrix Γ_{k-1} corrects various components of the noise process rather than deliver white noises. Thus, the performance of Kalman filter is suboptimal herein.

The measurement equation for Kalman filtering is expressed by:

$$\mathrm{Z}_k = \mathrm{H}\mathrm{X}_k + v_k \tag{46}$$

where Z_k is the difference between the estimate state ($\mathrm{V_N}$, $\mathrm{V_E}$, $\mathrm{V_D}$, L, λ, h) and the zero velocity and position reference ($\mathrm{V_{N,0}}$, $\mathrm{V_{E,0}}$, $\mathrm{V_{D,0}}$, $\mathrm{L_0}$, λ_0, $\mathrm{h_0}$):

$$\mathrm{Z}_k = \begin{bmatrix} \mathrm{V_N} - \mathrm{V_{N,0}} \\ \mathrm{V_E} - \mathrm{V_{E,0}} \\ \mathrm{V_D} - \mathrm{V_{D,0}} \\ \mathrm{L} - \mathrm{L_0} \\ \lambda - \lambda_0 \\ \mathrm{h} - \mathrm{h_0} \end{bmatrix} \tag{47}$$

$$\mathrm{H} = \begin{bmatrix} \mathrm{H_{11}} & \mathrm{H_{12}} & \mathrm{H_{13}} & \mathrm{H_{14}} & \mathrm{H_{15}} \\ \mathrm{H_{21}} & \mathrm{H_{22}} & \mathrm{H_{23}} & \mathrm{H_{24}} & \mathrm{H_{25}} \end{bmatrix} \tag{48}$$

where $\mathrm{H_{11}}$, $\mathrm{H_{13}}$, $\mathrm{H_{21}}$, $\mathrm{H_{22}}$ are 3×3 zero matrices, respectively; $\mathrm{H_{14}}$, $\mathrm{H_{15}}$ $\mathrm{H_{24}}$, $\mathrm{H_{25}}$ are 3×12 zero matrices, respectively; and $\mathrm{H_{12}}$, $\mathrm{H_{13}}$ are 3×3 unit matrices, respectively.

4. Results and Discussion

The test collects 60 s of stationary data to verify the algorithm and extracts the initial 5 s data for coarse alignment. The initial latitude, longitude and position are 45.77755°, 126.687898° and 124 m, respectively and the initial velocities are set to 0. Figure 11 shows original data outputs of the system.

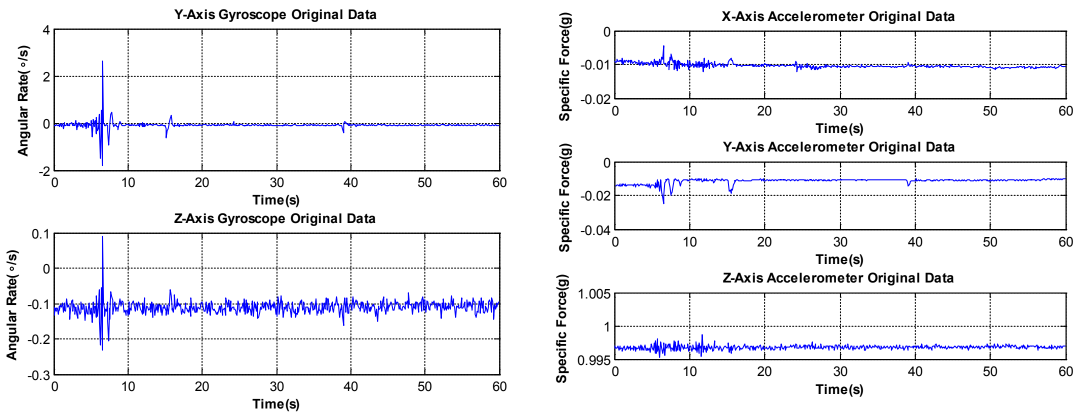

(**a**) (**b**)

Figure 11. (**a**) Two-axes gyroscope original data; and (**b**) three-axes accelerometer original data.

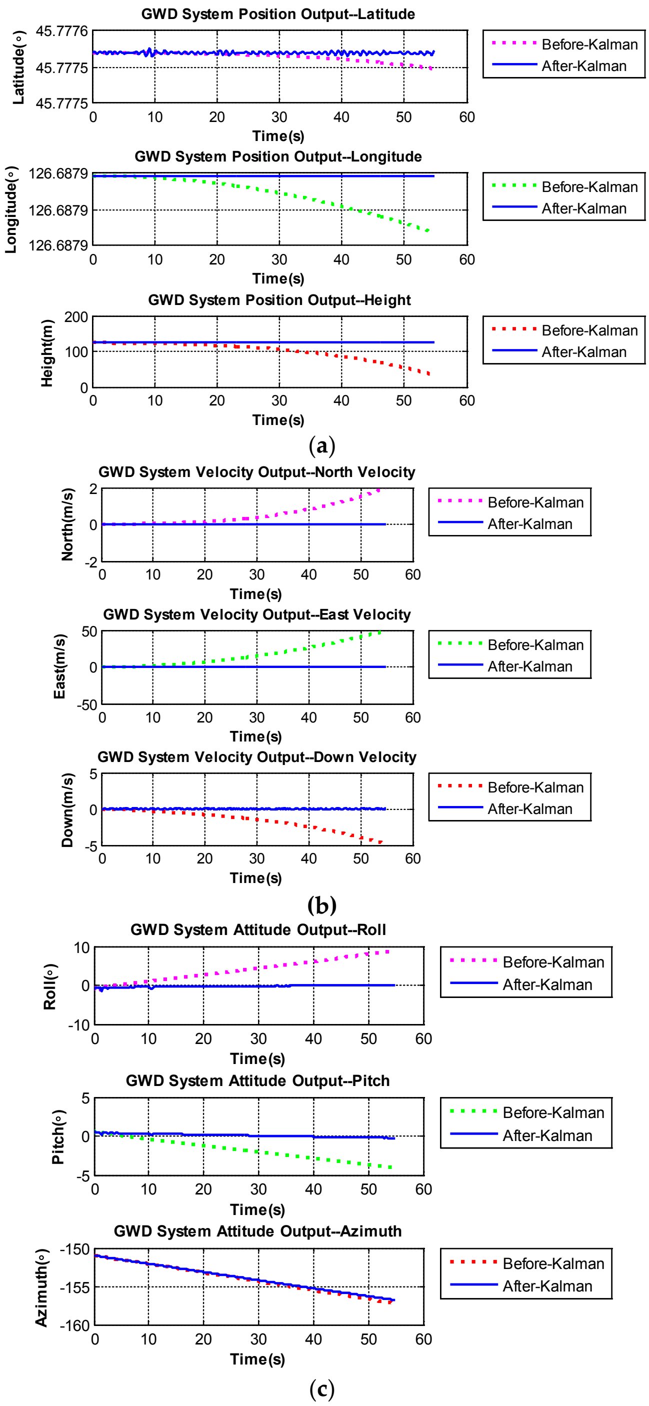

Figure 12. (**a**) MGWD system position solution with the Kalman filter; (**b**) MGWD system velocity solution with the Kalman filter; and (**c**) MGWD system attitude solution with the Kalman filter.

Figure 12a–c describes the MGWD system position, velocity, and attitude outputs obtained with the aid of zero velocity and position, which show that the Kalman filter can track the real position and velocity correctly. All diagonal values of the initial estimation error covariance are set to 0.01 and all diagonal values of the system noise covariance matrix are set to 1. The measurement noise covariance matrix is set as: $R = \mathrm{diag}\begin{bmatrix} 0.1 & 0.1 & 0.1 & 0.1 & 0.1 & 0.1 \end{bmatrix}$ and all initial system error states are set to 0. The maximum error for position, velocity and attitude between the mechanization outputs and the Kalman filter outputs are:, 2.4682×10^{-9}, $(2.6364 \times 10^{-11})^{\circ}$, 5.401×10^{-5}, 0.009 m/s, 0.0179 m/s, -5.5009×10^{-4} m/s, $(5.3521 \times 10^{-4})^{\circ}$, $(1.8512 \times 10^{-5})^{\circ}$, and $(4.6093 \times 10^{-7})^{\circ}$ Hence, for the attitude compensation, the zero velocity and position update approach cannot compensate for the azimuth error which drifts dramatically, as illustrated in Figure 13. Figure 13 shows attitude, velocity, and position estimation errors of: 0.0162°, −0.0073°, 0.0535°, 0.0043 m/s, 0.0093 m/s, −0.0032 m/s, $(-0.1902 \times 10^{-8})°$, $(-0.5976 \times 10^{-8})°$ and −0.0002 m. The above results imply that Kalman filtering can effectively restrain position, velocity, and attitude error, but not the azimuth error.

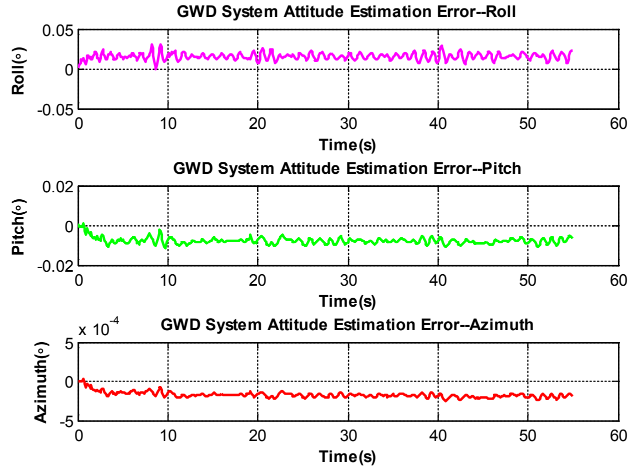

(**a**)

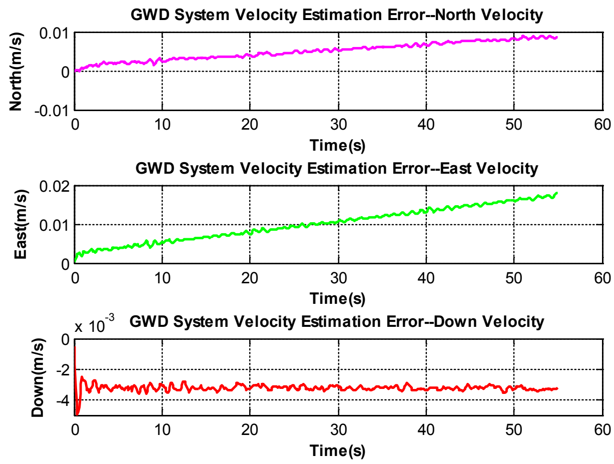

(**b**)

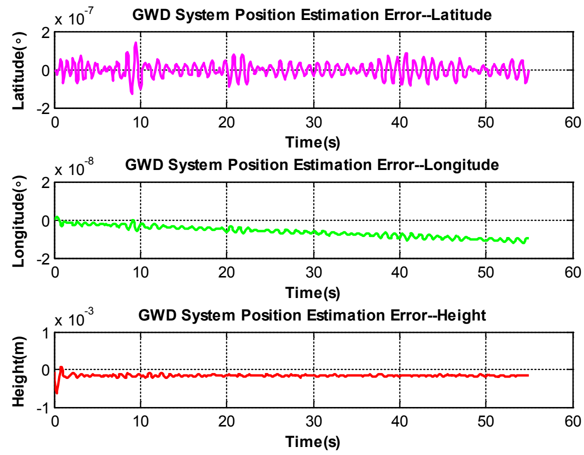

(**c**)

Figure 13. (**a**) Kalman filter position estimation error; (**b**) Kalman filter velocity estimation error; and (**c**) Kalman filter attitude estimation error.

Figure 14 show the standard deviations of the attitude estimation errors and the standard deviations of the velocity estimation errors, respectively. In Figure 14a the standard deviations of the roll and the pitch estimation errors converge to about 0.0348° and 0.0104°, respectively, while the standard deviation of the azimuth is divergent. The conclusion is that the state variables of the roll and the pitch are completely observable by the Kalman filter, but the state variable of the azimuth, is not observable. Similarly, the state variables (north, east, and down velocity) in the Kalman filter are completely observable and converge to 0.0277, 0.0292 and 0.0270 m/s, respectively as shown in Figure 14b.

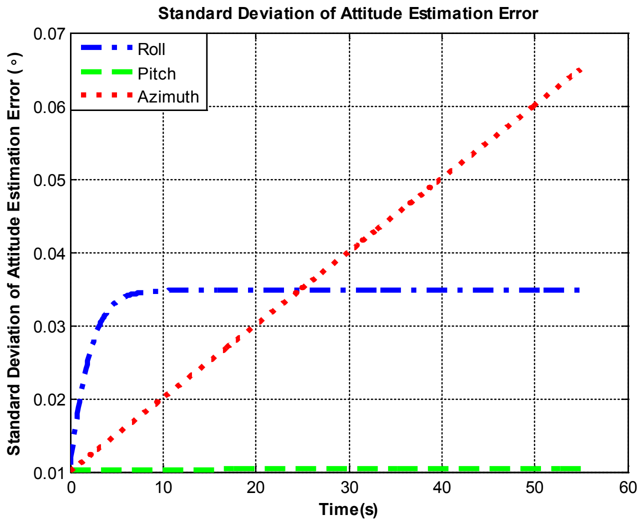

(**a**)

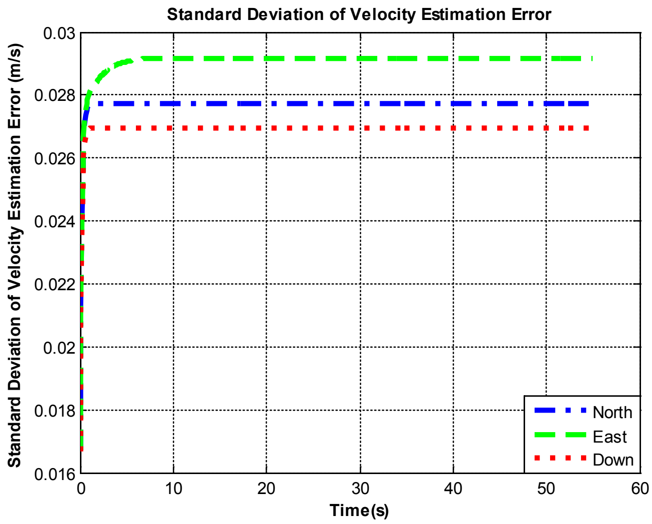

(**b**)

Figure 14. (**a**) Standard deviation attitude estimation error; and (**b**) standard deviation velocity estimation error.

As shown in Figure 15, the trace of the Kalman filter estimation error covariance matrix converges to 0.2 after 2 s. However, it is prone to drift because the azimuth error cannot be estimated in the Kalman filter. Additionally, the controllable and the observable matrices of the Kalman filter aided jointly by zero velocity and position updates are full rank. As a whole, the Kalman filter using zero velocity and position updates to compensate the MGWD system error with the fourth order AR model for statistical noise is convergent but drifts due to the azimuth error growth. Thus, as illustrated by Figure 14a, the standard deviation of the azimuth estimation error grows uncontrollably, and other observability-enhancing techniques, similar to IDA or R-IDA, should be sought in order for this technique to ever become applicable downhole. This presents a challenge for such miniature systems, since their pre-determined, dynamically-controlled motion can be achieved only by adding relatively complex motion-inducing and motion-assessing enclosures, which by themselves have to be prone to high temperatures and high vibrations, while at the same time being reasonably inexpensive and technologically easy to implement.

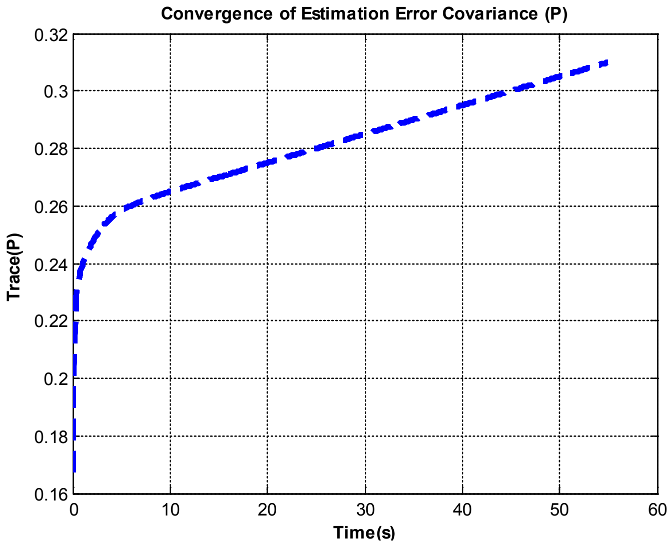

Figure 15. Convergence of the estimation error covariance.

5. Conclusions

This paper presents the design and the algorithm verification of a small-diameter MGWD system with reduced number of inertial sensors. In the reported design, small diameter, and high-temperature sensors are selected to meet MGWD system design requirements. The integrated MGWD data collection software can perform both real-time data display and post-processing for a complete navigation solution. Allan variance approach is selected to test sensor performance based on stochastic error modeling. In order to eliminate the stochastic error, a precise AR-based mathematical model is built. With the aid of a zero velocity and position update, quasi-stationary fine alignment can deliver the real attitude, velocity, and position tracking utilizing a Kalman filter that can effectively estimate system state with the employed augmented system state space model. In addition, the Kalman filter for system state estimation was determined to be convergent through evaluating the estimation error covariance matrix. However, the uncontrollable growth in the azimuth error cannot be compensated using this approach, and separate observability-enhancing mechanisms should be sought and integrated before such MGWD systems can really be applicable downhole.

Acknowledgments: This project was supported in part by the Natural Sciences and Engineering Research Council of Canada and the China Scholarship Council.

Author Contributions: The last author, Martin P. Mintchev, proposed the gyroscope-accelerometer based design approach for this paper. The first author Tao Li proposed the reduction of the number of gyroscopes and performed the reported experiments. Numerical simulations, and data processing were performed by Tao Li and Haiyu Lan. Gannan Yuan and Martin Mintchev supervised the entire work and provided important technical feedback. All four authors have contributed to the writing of the paper.

Conflicts of Interest: The original gyroscope-based downhole surveying idea has been patented by Martin P. Mintchev and his colleagues and is supported by Innovate Calgary Inc., Calgary, AB, Canada

Appendix A

The specific parameters of augmentation system state space model in Equation (43) list as following:

$$F_{\mathrm{fw},x} = \begin{bmatrix} 0 & 1 & 0 & 0 \\ 0 & 0 & 1 & 0 \\ 0 & 0 & 0 & 1 \\ -0.3308 & 0.0995 & -0.2036 & -0.3347 \end{bmatrix}$$

$$F_{\mathrm{fw},y} = \begin{bmatrix} 0 & 1 & 0 & 0 \\ 0 & 0 & 1 & 0 \\ 0 & 0 & 0 & 1 \\ -0.3307 & 0.1118 & -0.1956 & -0.3350 \end{bmatrix}$$

$$F_{\mathrm{fw},z} = \begin{bmatrix} 0 & 1 & 0 & 0 \\ 0 & 0 & 1 & 0 \\ 0 & 0 & 0 & 1 \\ -0.1249 & 0.0801 & -0.0382 & -0.0724 \end{bmatrix}$$

$$\beta_{\mathrm{f}x,0} = \begin{bmatrix} 0 & 0 & 0 & 0 \\ 0 & 0 & 0 & 0 \\ 0 & 0 & 0 & 0 \\ 0 & 0 & 0 & 0.0034 \end{bmatrix}$$

$$\beta_{\mathrm{f}y,0} = \begin{bmatrix} 0 & 0 & 0 & 0 \\ 0 & 0 & 0 & 0 \\ 0 & 0 & 0 & 0 \\ 0 & 0 & 0 & 2.0947 \times 10^{-4} \end{bmatrix}$$

$$\beta_{\mathrm{f}z,0} = \begin{bmatrix} 0 & 0 & 0 & 0 \\ 0 & 0 & 0 & 0 \\ 0 & 0 & 0 & 0 \\ 0 & 0 & 0 & 3.3090 \times 10^{-6} \end{bmatrix}$$

$$F_{\omega \mathrm{w},x} = \begin{bmatrix} 0 & 1 & 0 & 0 \\ 0 & 0 & 1 & 0 \\ 0 & 0 & 0 & 1 \\ 0.0866 & 0.5159 & 0.0947 & 0.1270 \end{bmatrix}$$

$$F_{\omega \mathrm{w},y} = \begin{bmatrix} 0 & 1 & 0 & 0 \\ 0 & 0 & 1 & 0 \\ 0 & 0 & 0 & 1 \\ 0.8466 & 0.1105 & -0.2948 & 0.1642 \end{bmatrix}$$

$$F_{\omega \mathrm{w},z} = \begin{bmatrix} 0 & 1 & 0 & 0 \\ 0 & 0 & 1 & 0 \\ 0 & 0 & 0 & 1 \\ 0.2683 & 0.0026 & -0.0192 & 0.3496 \end{bmatrix}$$

$$\beta_{\omega x,0} = \begin{bmatrix} 0 & 0 & 0 & 0 \\ 0 & 0 & 0 & 0 \\ 0 & 0 & 0 & 0 \\ 0 & 0 & 0 & 2.2871 \times 10^{-7} \end{bmatrix}$$

$$\beta_{\omega y,0} = \begin{bmatrix} 0 & 0 & 0 & 0 \\ 0 & 0 & 0 & 0 \\ 0 & 0 & 0 & 0 \\ 0 & 0 & 0 & 7.1662 \times 10^{-7} \end{bmatrix}$$

$$\beta_{\omega z,0} = \begin{bmatrix} 0 & 0 & 0 & 0 \\ 0 & 0 & 0 & 0 \\ 0 & 0 & 0 & 0 \\ 0 & 0 & 0 & 6.982 \times 10^{-8} \end{bmatrix}$$

References

1. Ledroz, A.G.; Pecht, E.; Cramer, D.; Mintchev, M.P. Fog-based navigation in downhole environment during horizontal drilling utilizing a complete inertial measurement unit: Directional measurement-while-drilling surveying. *IEEE Trans. Instrum. Meas.* **2005**, *54*, 1997–2006. [CrossRef]
2. Hill, D.; Neme, E.; Ehlig-Economides, C.; Mollinedo, M. Reentry drilling gives new life to aging fields. *Oilfield Rev.* **1996**, *8*, 4–17.
3. Pendleton, L.E. Horizontal drilling review. In *Archie Conference on Reservoir Definition and Description*; Society of Petroleum Engineers: Houston, TX, USA, 1991; p. 6.
4. Longbottom, J.R.; Jano, J.C.; Cox, D.C.; Welch, W.R.; White, P.M.; Nivens, H.W.; Jacquier, R.C.; Holbrook, P.D.; Freeman, T.A.; Mills, D.H. Multilateral Well Drilling And Completion Method and Apparatus. EN Patent number EP0701045 A2, 15 October 1996.
5. Von Flatern, R. Operators are Ready for More Sophisticated Multilateral Well Technology. Available online: http://www.researchgate.net/publication/255035866_Operators_are_ready_for_more_sophisticated_multilateral_well_technology (accessed on 2 December 2015).
6. Wang, Z. Mems-Based Downhole Inertial Navigation Systems for Directional Drilling Applications. Master's Thesis, University of Calgary, Calgary, AB, Canada, 2015.
7. Ishak, I.B.; Macaulay, R.C.; Stephenson, P.M.; Al Mantheri, S.M. Review of horizontal drilling. In *Middle East Oil Show*; Society of Petroleum Engineers: Manama, Bahrain, 1995.
8. Matheson, E.; Lee, R.G.M. The first use of gravity MWD in offshore drilling delivers reliable azimuth measurements in close proximity to sources of magnetic interference. In Proceedings of the IADC/SPE Drilling Conference, Dallas, TX, USA, 2–4 March 2004.
9. Zijsling, D.H.; Wilson, R.A. Improved Magnetic Surveying Techniquesfield Experience. In *Offshore Europe*; Society of Petroleum Engineers: Aberdeen, UK, 1989.
10. Noureldin, A.; Irvine-Halliday, D.; Mintchev, M.P. Accuracy limitations of fog-based continuous measurement-while-drilling surveying instruments for horizontal wells. *IEEE Trans. Instrum. Meas.* **2002**, *51*, 1177–1191. [CrossRef]
11. Torgeir, T.I.E.; Fjogstad, A.; Saasen, A.; Amundsen, P.A.; Omland, T.H. Drilling fluid affects MWD magnetic azimuth and wellbore position. In Proceedings of the IADC/SPE Drilling Conference, Dallas, TX, USA, 2–4 March 2004.
12. Cheatham, C.A.; Shih, S.; Churchwell, D.L.; Woody, J.M.; Rodney, P.F. Effects of magnetic interference on directional surveys in horizontal wells. In Proceeding of SPE/IADC Drilling Conference, New Orleans, LA, USA, 18–21 February 1992.
13. Savage, P.G. *Strapdown Analytics*; Strapdown Associates, Inc.: Maple Plain, MN, USA, 2000; Volume 1.
14. Britting, K.R. *Inertial Navigation Systems*; Wiley-Interscience: New York, NY, USA, 1971; p. 249.
15. Edvardsen, I.; Nyrnes, E.; Johnsen, M.G.; Hansen, T.L.; Løvhaug, U.P.; Matzka, J. Improving the accuracy and reliability of MWD magnetic wellbore directional surveying in the Barents Sea. In Proceedings of the SPE Annual Technical Conference and Exhibition, Oreleans, LA, USA, 30 September–2 Ocotber 2013.
16. Van Nispen, J.; Howe, N.A. Directional surveying using inertial techniques—Field experience in the northern north sea. In Proceedings of the SPE Offshore Europe, Aberdeen, UK, 15–18 September 1981.

17. Noureldin, A.; Tabler, H.; Irvine-Halliday, D.; Mintchev, M. Testing the applicability of fiber optic gyroscopes for azimuth monitoring for measurement-while-drilling processes in the oil industry. In Proceedings of the Position Location and Navigation Symposium, Atlanta, GA, USA, 22–26 April 2000; pp. 291–298.
18. Uttecht, G.W.; de Wardt, J.P. Application of small-diameter inertial grade gyroscopes significantly reduces Borehole position uncertainty. In Proceedings of the IADC/SPE Drilling Conference, New Orleans, LA, USA, 20–23 February 1983.
19. Elgizawy, M.; Noureldin, A.M.; El-Sheimy, N. MEMS gyroscope-while-drilling environment qualification testing. In Proceedings of the IADC/SPE Drilling Conference and Exhibition, New Orleans, LA, USA, 2–4 February 2010.
20. Richardson, D.A. A gyroscope guidance sensor for ultra-deepwater applications. In Proceedings of the Offshore Technology Conference, Houston, TX, USA, 2–5 May 2014.
21. Noureldin, A. *New Measurement-While-Drilling Surveying Technique Utilizing Sets of Fiber Optic Rotation Sensors*; University of Calgary: Calgary, AB, Canada, 2002.
22. Pecht, E.; Mintchev, M.P. Observability analysis for ins alignment in horizontal drilling. *IEEE Trans. Instrum. Meas.* **2007**, *56*, 1935–1945. [CrossRef]
23. Shin, E.-H. *Accuracy Improvement of Low Cost INS/GPS for Land Applications*; University of Calgary: Calgary, AB, Canada, 2001.
24. Mintchev, M.P.; Pecht, E.; Cloutier, J.; Dzhurkov, A. In Drilling Alignment. U.S. Patent 7823661 B2, 2 November 2010.
25. Jurkov, A.S.; Cloutier, J.; Pecht, E.; Mintchev, M.P. Experimental feasibility of the in-drilling alignment method for inertial navigation in measurement-while-drilling. *IEEE Trans. Instrum. Meas.* **2011**, 1088–1089. [CrossRef]
26. Wang, Z.; Poscente, M.; Filip, D.; Dimanchev, M.; Mintchev, M. Rotary in-drilling alignment using an autonomous mems-based inertial measurement unit for measurement- while-drilling processes. *IEEE Trans. Instrum. Mag.* **2014**, *16*, 26–34. [CrossRef]
27. Titterton, D.H.; Weston, J.L. *Strapdown Inertial Navigation Technology*, 2nd ed.; American Institute of Aeronautics and Astronautics: New York, NY, USA, 2004.
28. Oy, M.E. Scc1300-d04 Combined Gyroscope and 3-Axis Accelerometer with Digital Spi Interfaces. Available online: http://www.murata.com/~/media/webrenewal/products/sensor/gyro/scr1100/scr1100-d04%20datasheet%20v2%201.ashx?la=en-us (accessed on 25 November 2015).
29. Noureldin, A.; Tabler, H.; Smith, W.; Irvine-Halliday, D.; Mintchev, M.P. Continous Measurement-While-Drilling Surveying. U.S. Patent No. 6823602 B2, 5 September 2003.
30. Groves, P.D. *Principles of Gnss, Inertial, and Multisensor Integrated Navigation System*; Artech House: Boston, MA, USA; London, UK, 2008; p. 505.
31. El-Sheimy, N. Dynamic Error State Model. In *Inertial Techniques and INS/DGPS Integration: Derivation of the INS*; ENGO 623-Course Note; University of Calgary: Calgary, AB, Canada, 2006; pp. 3–5.
32. Brian D.O. Anderson, J.B.M. *Optimal Filter*; Prentice Hall Inc.: EngleWood Cliffs, NJ, USA, 1979.
33. Simon, D. *Optimal State Estimation: Kalman, H Infinity, and Nonlinear Approaches*; John Wiley and Sons, Inc: Hoboken, NJ, USA, 2006.
34. Bar-Shalom, Y.; Rong, X.L.; Kirubarajan, T. *Estimation with Applications to Tracking and Navigation*; John Wiley and Sons, Inc.: Toroto, ON, Canada, 2001; p. 188.
35. Wu, Y.; Zhang, H.; Wu, M.; Hu, X.; Hu, D. Observability of strapdown ins alignment: A global perspective. *IEEE Trans. Aerosp. Electron. Syst.* **2012**, *48*, 78–102.
36. Moore, B. Principal component analysis in linear systems: Controllability, observability, and model reduction. *IEEE Trans. Autom. Control* **1981**, *26*, 17–32. [CrossRef]
37. IEEE. *IEEE Standard Specification Format Guide and Test Procedure for Single-Axis Interferometric Fiber Optic Gyros*; Standard 952-1997; IEEE: New York, NY, USA, 1998.
38. Nassar, S. *Improving the Inertial Navigation System (INS) Error Model for Ins and Insdgps Applications*; University of Calgary: Calgary, AB, Canada, 2003.
39. Quinchia, A.G.; Falco, G.; Falletti, E.; Dovis, F.; Ferrer, C. A comparison between different error modeling of mems applied to GPS/INS integrated systems. *Sensors* **2013**, *13*, 9549–9588. [CrossRef] [PubMed]
40. Gelb, A. *Applied Optimal Estimation*; The MIT Press: Cambridge, MA, USA, 1974; p. 382.

41. Von Storch, H.; Zwiers, F.W. *Statistical Analysis in Climate Research*; Cambridge University Press: Cambridge, UK, 2002; p. 496.
42. El-Sheimy, N. *Inertial Techniques and INS/DGPS Integration: Initial Alignment of INS*; ENGO 623-Course Note; University of Calgary: Calgary, AB, Canada, 2006; p. 43.
43. Jiang, Y.F. Error analysis of analytic coarse alignment methods. *IEEE Trans. Aerosp. Electron. Syst.* **1998**, *34*, 334–337. [CrossRef]
44. Noureldin, A.; Karamat, T.B.; Eberts, M.D.; El-Shafie, A. Performance enhancement of mems-based INS/GPS integration for low-cost navigation applications. *IEEE Trans. Veh. Technol.* **2009**, *58*, 1077–1096. [CrossRef]